Received 15 November 2020,
Accepted 8 January, 2021
https://doi.org/10.1016/j.fuel.2021.120196

preprint for final article published: *Fuel 291 (2021) 120196*

Evolution in size and structural order for incipient soot formed at flame temperatures greater than 2100 K

Shruthi Dasappa[a,b] and Joaquin Camacho [*a]

Soot formed in flames hotter than conventional combustion applications is expected to undergo unique formation processes and develop a carbon structure distinct from typical soot. A complementary experimental and modeling approach is reported here to assess flame temperature and equivalence ratio effects for soot formed in the higher-temperature regime (1950 K < T_f < 2250 K). Computations using three separate combustion chemistry models show that predictions of polycyclic aromatic hydrocarbon (PAH) concentration profiles for the higher-temperature flames are more sensitive to the choice in mechanism rather than specific flame conditions. As for material properties, the Raman signatures transition from a typical soot spectrum to features observed in disordered sp^2 carbon materials. The defect distance extracted from the Raman bands nearly doubles from values typically reported for soot as the flame temperature exceeds 2200 K. Higher concentrations of gas-phase precursors may facilitate development of an ordered carbon structure as indicated by the relatively high defect distance observed for the highest equivalence ratio series. Particle size distributions measured by mobility sizing show size and yield of soot decreases with increasing flame temperature and the bimodal distribution falls within the ultra-fine range for all flame conditions. This is especially promising if the significant transformation in carbon structure inferred from the evolution in Raman spectra enables development of functional high-surface area sp^2 carbon materials. Namely, the current observations indicate that the flame-formed carbon structure evolves towards high-defect sp^2 carbon with size and carbon structure that can be tuned to some extent.

[a] *Mechanical Engineering Department, San Diego State University, San Diego, CA USA*
[b] *Mechanical and Aerospace Engineering Department, University of California San Diego, San Diego, CA, USA*

1. Introduction

Soot formation remains an unavoidable combustion problem affecting performance [1], public health [2] and the environment [3]. Interestingly, flame-formed carbon also has a long history as a useful material [4,5]. The current work focuses on the production of flame-formed carbon nanoparticles in flames hotter than typical combustion applications. Processes designed for flame temperatures much greater than typical engines include rocket propulsion [6], oxy-fuel combustion [7] and enriched / preheated air applications [8]. A complementary experimental and modeling approach focusing on this temperature range is taken to shed light on distinctive higher-temperature (T > 2100 K) soot formation processes. Soot yield is known to decrease at elevated flame temperatures [9–12] but systematic studies of particle size distribution, carbon structure and other detailed properties rarely venture beyond 2100 K. Investigation of soot formed in this regime is relevant to higher-temperature combustion applications and characterization of the carbon structure may reveal unique and potentially useful properties.

Evolution in soot particle size distribution and carbon bonds are examined here in laminar stretch-stabilized flames having maximum flame temperatures hotter than previously reported. Premixed stretch-stabilized flames have been shown [13,14] to be an effective flame configuration for investigating fundamental soot formation processes close to the adiabatic flame temperature. The pseudo one-dimensional configuration enables systematic study of detailed processes in a flow-field amenable to computational reacting flow modeling [13,15]. A series of flame experiments is established in the current work for isolation of the equivalence ratio and flame temperature effects on soot formation in the higher-temperature regime. Computation of the flame structure is also carried out for insight into the growth conditions in terms of the temperature-time history and polycyclic aromatic hydrocarbon (PAH) precursors. Elevated temperature is known to cause a decrease in soot precursor production [16,17], a decrease in particle collision efficiency [18,19] and an increase in particle carbonization rate [20–22].

Raman spectra of carbon deposited from flames at increasing flame temperature and equivalence ratio are analyzed to observe increase carbon structural ordering under a range of fuel-rich conditions. Raman spectroscopy is a valuable tool for probing carbon structure and elucidating soot properties such as absorption cross-section [23], optical band gap [24], and crystallite size [25]. A wealth of knowledge has been obtained from analysis of Raman spectra for soot formed in premixed flames [26–32], diffusion flames [25,26,33–36], and engines [37,38]. Although the range of flame conditions is large, the characteristics of the Raman spectra fall within a narrow range. That is to say, the nature of sp^2 bonding, sp^3 bonding and crystallite size do not change drastically under the conventional range of sooting flame conditions. In contrast, the authors have

previously reported a transformation in the Raman signature for flame-formed carbon in the higher-temperature regime [14]. Rather than subtle changes to the characteristic D and G peaks of the Raman spectra, a dramatic shift in the relative heights and widths occurs as the flame temperature increases beyond 2100 K. If the correlation of Ferrari for highly defective graphite is applied [39,40], the evolution in Raman spectra indicates that the distance between crystalline defects becomes significantly larger with increasing temperature. This analysis is expanded upon in the current work to assess flame-formed carbon at increasing equivalence ratio in terms of defect density for the higher-temperature regime.

The flame conditions currently studied correspond to formation of incipient soot at the earliest growth stages. High-surface area carbon nanoparticles corresponding to freshly formed soot is expected, but, the relatively high flame temperature may also induce carbonization only observed in so-called "mature" soot. In fact, the unique combination of "young", nucleation sized particles having relatively low defect density may be useful for applications of functional carbon black and hard carbon. Characterization of particle formation processes and material properties for flame-formed carbon will shed light on the higher-temperature regime and inform potential applications of the material produced.

2. Materials and Methods

2.1 Computational - A series of stretch-stabilized ethylene-oxygen-argon flames is designed to track the effect of increasing flame temperature and equivalence ratio on flame-formed carbon size and structure. These flames are stabilized in a laminar stagnation flow with a steady position given by the balance between the decelerating convective velocity and opposing local flame speed [41]. A summary of the flames studied is shown in Table 1 with a more detailed table given as supplementary material. For a given equivalence ratio, Φ , the flame temperature and flame position are tuned by the flame diluent argon concentration, X_{Ar} and total flow rate. The use of argon instead of nitrogen enables higher flame temperatures to be established due to the heat capacity effect. Flame structure computations, carried out by OPPDIF [42], are used to guide the design of the flame series and to gain insight into the growth conditions of the flame-formed carbon. The pseudo one-dimensional formulation taken in OPPDIF is most accurate for domains in which the nozzle diameter is much greater than the nozzle-to-stagnation surface distance [43–45]. In some cases, however, OPPDIF was recently shown to perform as a fast and reasonably accurate approach for flame structure calculation even for more narrow aspect ratio domains [46].

OPPDIF is used to determine the maximum flame temperature, $T_{f,max}$, and particle growth time, t_p , for a given inlet composition and flow rate. The particle growth time is given by the time for a Lagrangian particle to travel from the location of the flame zone to the stagnation surface location. Carbon particles are assumed to follow the gas convective velocity until the thermophoretic force induces additional drift towards the colder stagnation surface. See previous work for more details on the OPPDIF and thermophoretic velocity computations [13,47]. Flame series for Φ = 2.4, 2.5 and 2.6 with increasing flame temperature (1950 K < $T_{f,max}$ < 2250 K) and comparable growth time are established. Soot formation processes are not considered in the flame modeling study carried out here. Rather, detailed combustion chemistry models are used to determine the flame structure in the absence of soot. USC Mech II [48] is used as a baseline model (foundational chemistry up to benzene) to calculate the flame structure as previous work showed relatively accurate prediction of measured flame structure compared to other models applied to sooting stretch-stabilized flames [13]. Separate flame computations are also carried out with combustion chemistry models incorporating PAH to assess soot precursor predictions. Computations for each flame using the KAUST PAH Mechanism 2 (KM2) [49], Appel, Frenklach, Bockhorn (ABF) [50] and Blanquart, Pepiot, Pitsch (BPP) [51] mechanisms are performed to provide a comparison of PAH predictions among the three models for the flames of interest. The KM2 mechanism is a gasoline surrogate mechanism built from USC Mech II foundational chemistry [49,52]. ABF is a classic mechanism for PAH chemistry based on GRI-Mech 3.0 foundational chemistry [53]. The BPP mechanism was developed for engine relevant fuels with GRI-Mech 3.0 foundational chemistry incorporating several updates [51] beyond the original GRI-Mech 3.0. Experimental PAH measurements do not exist in the higher-temperature regime and are beyond the current scope. As such, the computed PAH profiles provide insight into agreement among models that are extrapolated to higher temperature.

2.2 Experimental - The experimental flame configuration centers upon laminar, premixed stretch-stabilized flames in a setup similar to a previous study [14]. The unburned mixture issues from an aerodynamically shaped nozzle (D_{nozzle} = 1.43 cm) to induce a plug-flow such that the experiment approaches the inlet boundary condition assumed in OPPDIF. A steady ethylene-oxygen-argon flame is stabilized between the nozzle and a water-cooled stagnation surface. The nozzle-to-stagnation surface distance is L = 2.54 cm for all flames studied but each flame has a different standoff distance designed for comparable particle time across all flames. With a fixed nozzle-to-stagnation surface distance, the flame position (standoff distance) is controlled by adjusting the total flow rate of the unburned gases to manipulate the balance between the flow velocity and laminar flame speed. A concentric flow of nitrogen shrouds the flame to reduce perturbation from the surrounding environment. The temperature at the nozzle and stagnation surface boundary are monitored by type K thermocouples with temperatures maintained at T_{nozzle} = 330 ± 20 K and $T_{stagnation}$ = 400 ± 20 K. Calibrated critical orifices are used to control all gas flow rates.

A Thermo DXR2 Raman Microscope with a 532 nm excitation source is used to obtain spectra of the as-deposited films. The laser is focused under a 50x objective at 1 mW power and care was taken to prevent modifications to the carbon structure by excessive laser excitation. Characterization by Raman spectroscopy is done off-line by analyzing carbon particle films deposited onto an aluminum substrate mounted to an aluminum water block. The axisymmetric flame (pictured in Fig. 1) is a stagnation flow impinging on the flat, water-cooled stagnation surface. Thin (2 mm) aluminum plates are mounted flush with this surface as the flame-formed carbon deposits and coats the plate over time. Aerosol sampling is carried out in separate experiments where the deposition plates are replaced with a flat plate embedded with a thin-wall (125 micron) cross-

flow sampling tube. Mobility particle sizing for the soot particle size distribution function (PSDF) is carried out by aerosol sampling from a micro-orifice ($D_{orifice}$ = 130 microns) embedded flush with the flat plate assembly. Previously established sampling methods [47,54], are applied to minimize artifacts to the measured distribution due to diffusion losses and sampling-induced particle coagulation.

$T_{f,max}$ (K)	t_p (ms)	v_o (cm/s)	X_{Ar}
C_2H_4-O_2-Ar , ϕ = 2.4 series			
2035	18	91	0.69
2085	15	101	0.67
2110	15	98	0.66
2140	15	97	0.65
2190	14	90	0.63
2240	14	86	0.61
C_2H_4-O_2-Ar , ϕ = 2.5 series			
1980	14	104	0.68
2015	18	87	0.67
2080	16	90	0.65
2150	13	101	0.62
2195	13	97	0.60
2260	12	88	0.57
C_2H_4-O_2-Ar , ϕ = 2.6 series			
1950	18	91	0.67
2050	16	95	0.65
2080	16	86	0.62
2110	16	83	0.61
2135	16	80	0.59
2205	14	79	0.55

$T_{f,max}$ computed using OPPDIF with measured boundary conditions: separation distance, L = 2.54 cm, T_{nozzle} = 330 K and $T_{stagnation}$ = 400 K. t_p is based on OPPDIF computed flame structure with thermophoretic velocity given by the hard sphere limit. v_o is cold gas velocity.

A TSI 1 nm Scanning Mobility Particle Sizer (TSI 3838E77) consisting of a dual voltage classifier (TSI 3082), a Kr-85 bi-polar diffusion charger (Neutralizer TSI 3077A), 1 nm differential mobility analyzer (DMA) (TSI 3086), a diethylene glycol-based (DEG) condensation particle counter (CPC) (so-called Nanoenhancer, TSI 3777) and a butanol-based CPC (TSI 3772) is used in the "compact" configuration recommended by the vendor to minimize diffusion loss of small particles. See previous work for more details and schematics of the mobility sizing and carbon deposition setups [14]. TSI Aerosol Instrument Manager Software (version 10.2) is used to collect and export the measured PSDFs. An insert supplied by the vendor is now mounted onto the inlet of the neutralizer to minimize flow recirculation for more predictable attainment of the equilibrium charge distribution. TSI also measured the penetration of ultra-fine particles through the system flow path recently and a new diffusion loss correction [55] is applied to the measured PSDF. The mobility size is corrected to properly account for the transition in gas-particle collision regimes for ultra-fine soot particles [56].

Color-ratio pyrometry is carried out to analyze radiative emissions of the flame-formed carbon *in-situ*. A commercial DSLR camera (NIKON D3400) with the infrared filter removed is used to capture RAW images of the axisymmetric flame projection. Three separate images of the steady flame are recorded with bandpass filters (Andover FS20) for λ = 450 nm, 650 nm and 900 nm mounted to the lens provide three color ratios. Analysis is performed on an average of 10 frames and an Abel transform is used to convert the projection into an axisymmetric radial profile. The current technique is based on the method introduced by Sunderland and co-workers [57] with an additional modification to account for the evolution of optical properties as the soot structure evolves through the flame. Gomez and co-workers recently captured the evolution in particle radiative intensity in terms of the dispersion exponent, α , by assuming soot emissivity is proportional to $\lambda^{-\alpha}$ [58]. Applying this assumption, the measured color ratio could be interpreted in terms of Planck's Law as follows:

$$\frac{GS_{\lambda 1}}{GS_{\lambda 2}} = \frac{b_1\,\tau_1\,\Delta\lambda_1\,\lambda_2^{5+\alpha}\,exp\left(\frac{hc}{\lambda_2 kT}\right)}{b_2\,\tau_2\,\Delta\lambda_2\,\lambda_1^{5+\alpha}\,exp\left(\frac{hc}{\lambda_1 kT}\right)} \qquad \text{eq. 1}$$

where $\mathrm{GS}_i(r)$ is the greyscale output for the filtered camera sensor after transformation to a radial profile, b_i is the wavelength specific calibration constant relating the filtered camera sensor response to blackbody spectral intensity, c is the speed of light, h is the Planck's constant, k is the Boltzmann's constant, T is the temperature of the particle (assumed to be equal to the surrounding gas), λ_i is the rated wavelength of the bandpass filter, τ_i is the transmissivity of the filter and $\Delta\lambda_i$ is the full width at half maximum (FWHM) of the bandpass. b_i is calibrated using a blackbody furnace (Newport Oriel 67032) while confirming the linear response of the camera sensor to intensity for a range of exposure times. The camera and filter properties are known, but the particle (flame) temperature could only be independently measured in this formulation if the particle dispersion exponent, α, is also known. For soot, a range of $0.5 < \alpha < 4$ has been reported depending on the specific flame and experimental conditions [58–64].

3. Results and discussion

Evolution in carbon structure and size distribution is observed experimentally to examine unique soot formation behavior at flame temperatures greater than conventional combustion applications. Complementary flame structure calculations provide insight into particle temperature-time history and gas-phase soot precursors. Soot modeling is beyond the scope of the current work as PAH chemistry, collision efficiency, particle carbonization and other processes must be established in the higher-temperature regime before reliable soot formation models could be developed. Computational flame structure results obtained by OPPDIF are shown in Fig. 1

for the centerline of the Φ = 2.6, $T_{f,max}$ = 2205 K case. An image of this flame is also shown as representation of the sooting premixed stretch-stabilized flames currently studied. The position of the flame front is distinguished in flame images by the onset of luminosity. In the computations, the flame position is associated with sharp features of the computed flame structure such as a temperature rise, a velocity increase and a narrow peak of combustion intermediates . Particle inception occurs immediately after the flame zone as evidenced by the observed yellow luminosity next to the blue flame disc. The flame-formed particles then grow in the post-flame region and eventually deposit onto the stagnation surface. The flame conditions chosen in the current work are designed to isolate flame temperature and equivalence ratio effects for comparable particle times. Accompanying color-ratio pyrometry experiments are used to assess the consistency of the flame structure calculations.

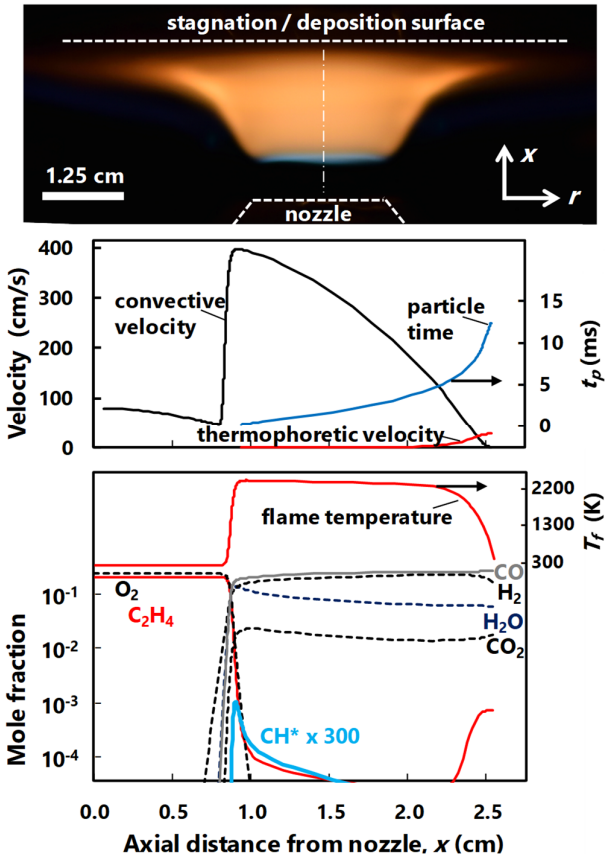

Figure 1: Flame image (top), computed centerline axial profiles for velocity and particle time (middle) and flame temperature and major species (bottom) for the Φ = 2.6, $T_{f,max}$ = 2205 K flame case.

The temperature profile is fixed to match the flame structure solution from USC Mech II for all comparisons between PAH mechanisms. The flame temperature predicted for stretch-stabilized flames is not primarily sensitive to a given fuel mechanism employed, but the flame position does strongly depend on the fuel kinetics. This effect is demonstrated in the supplementary material (Fig. S1) in terms of computed flame temperature profiles obtained by independently solving the energy equation for each combustion mechanism flame calculation. Substantial differences in computed flame position are observed among the PAH mechanisms due to deviations in ethylene combustion chemistry leading to differences in predicted fuel burning velocity. The USC Mech II based solution has been shown to predict the measured flame position in previous studies of sooting stretch-stabilized flames [13]. As such, the flame structure solutions for the three PAH mechanisms are constrained here to adopt the flame temperature profile from USC Mech II rather than independently solving the energy equation. Assessment of this assumption is carried out below by comparing flame position predicted by USC Mech II to the measured flame position of the current flames. The KM2 mechanism is a PAH flame chemistry model based on foundational chemistry taken from USC Mech II. As such, the agreement in measured flame temperature and position between USC and KM2 mechanisms is expected.

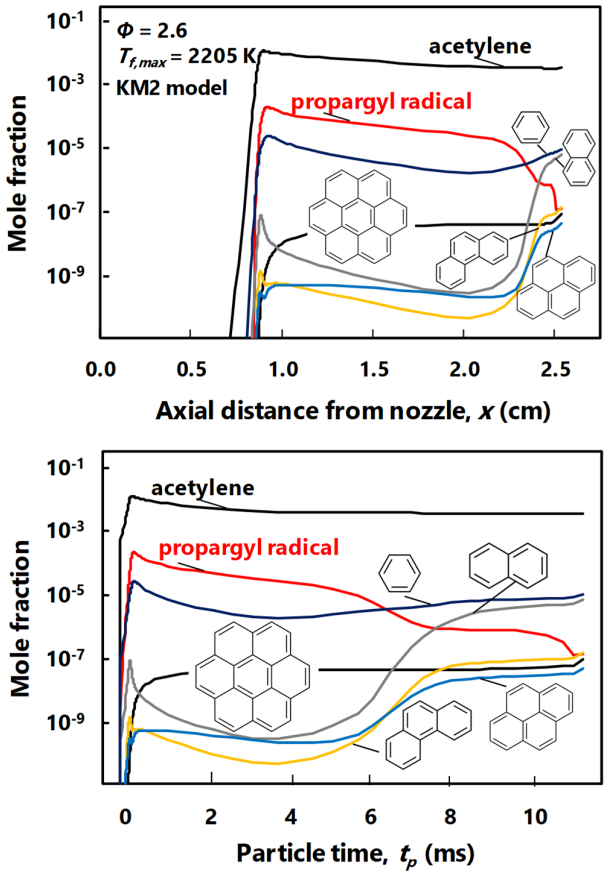

Figure 2: Computed gas-phase soot precursor profiles in terms of axial position (top) and particle time (bottom) based on the KM2 combustion chemistry model for the Φ = 2.6, $T_{f,max}$ = 2205 K flame case.

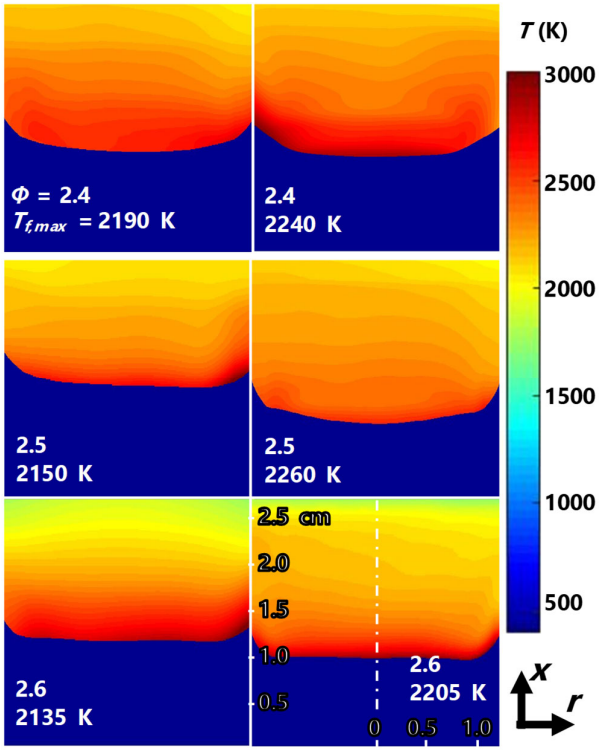

Figure 3: Axisymmetric flame temperature field, T_f (x,r) extracted from measured color-ratio field for α = 1.

The flame position and particle time is fixed across all models by imposing the USC Mech II based temperature profile in the OPPDIF computations running the KM2, ABF and BPP mechanisms. An example set of computed species profiles for soot precursors shown in Fig. 2 as a function of space and particle time. The profiles shown in Fig. 2 are the same flame conditions shown in Fig. 1 using KM2 chemistry and the constrained temperature profile. Non-monotonic profiles are predicted for the computed PAH concentrations. A sharp rise occurs in the flame zone where the fuel is converted to PAH due to fuel-rich kinetic processes. The subsequent drop and rise seen in post-flame region is primarily governed by equilibrium effects. Equilibrium PAH concentrations typically peak at moderate flame temperatures and decrease for relatively hot flames [65]. The flame temperature profile computed here evolves from high to low temperature as the burned gases approach the water-cooled stagnation surface. This causes a corresponding shift in equilibrium PAH concentrations. The temperature gradient in the vicinity of the water-cooled stagnation surface also induces thermal diffusivity of large and small gas phase species, which is a secondary cause for minor, additional shifts in the concentration

Constraining the temperature profile to the USC Mech II solution allows for PAH predictions to be assessed for the three models under comparable conditions. Another parameter governing flame structure is the unburned gas temperature as this impacts the adiabatic flame temperature of the mixture and the temperature dependent burn rate [13,41,66]. This effect is demonstrated in the supplementary material (Fig. S2) for computed PAH profiles based on the KM2 mechanism. The flame position moves closer to the nozzle and flame temperature increases for an increase in unburned gas temperature (T_{nozzle}) and the opposite effect occurs for lower unburned gas temperature. The flame structure is relatively insensitive to moderate changes in the stagnation plate temperature as was demonstrated in computational [67–71] and experimental studies [72–74]. The concentration profiles shift in with a change in flame temperature. As shown in Fig. S2, acetylene concentration increases in the post-flame region for the colder flame case and this may explain the corresponding increases for benzene, phenanthrene and pyrene observed.

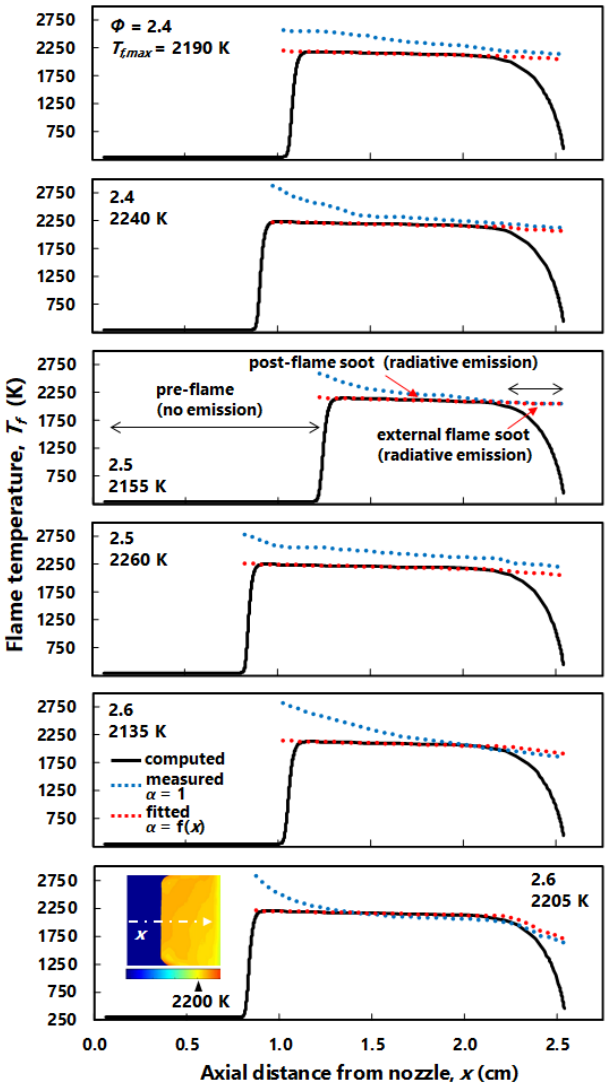

Figure 4: Measured and computed axial temperature profiles at the centerline. The measured profiles are shown for α = 1 and for α(x) fitted to match the computed temperature profile. The inset shows the measured temperature field for the Φ = 2.4, $T_{f,max}$ = 2205 K case determined using the fitted α(x) profile.

Color-ratio pyrometry measurements provide insight into the consistency of OPPDIF and USC Mech II for computing flame

structure in the higher-temperature regime. Measured temperature fields are shown in Fig. 3 for the two hottest flame conditions of each equivalence ratio. The temperature reported in Fig. 3 is based on the assumption that the particle emissivity is proportional to λ^{-1} which is a typical dispersion exponent applied to mature soot [57]. Under this assumption, the measured maximum temperature is much greater than the maximum computed by OPPDIF. The observed discrepancy and the axial variation in measured flame temperature may be due to evolution in soot particle properties rather than an actual property of the measured flame structure. Gomez and co-workers recently showed [58,61] that evolution in soot particle properties should be considered when interpreting radiative emissions from incipient soot. In the current flames, soot is expected to form close to the flame-front and grow over time as the C/H ratio and carbon structure also evolve. This evolution is also expected to depend on the particle temperature-time history and gas-phase environment (temperature and equivalence ratio effects).

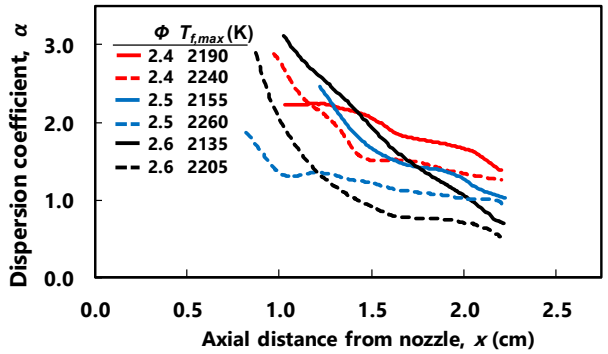

Figure 5: Dispersion exponent profiles based on fitting measured centerline radiative emission profiles to the computed axial flame temperature profile.

An independent temperature diagnostic would shed light on the current interpretation of measured particle radiative emissions for extracting flame temperature. Thermocouple measurements are simple and readily accessible, but this method is not reliable for stretch-stabilized flames as the aerodynamic balance would be heavily disturbed by flame anchoring onto thermocouple wires. As such, development of an alternate non-intrusive diagnostic to complement color-ratio pyrometry will be left for future work. In the absence of an independent diagnostic, the computed flame temperature profile is used to gain insight into the measured radiative intensity and flame temperature. A summary of comparisons between the measured and computed axial, centerline temperature profiles is shown in Fig. 4. Soot radiative emissions are detected in the post-flame region of the domain. The position where emissions are first detected above the nozzle coincide fairly closely with the flame position predicted by USC Mech II. The sharp rise in computed flame temperature overlaps the start of the emission profile or falls within 1 mm.

Flame temperature in the post-flame region of stretch-stabilized flames is expected to approach the adiabatic flame temperature with minor deviations based on strain, radiation and Lewis number effects [41]. The computed flame structure predicts this behavior with a plateau in flame temperature for most of the post-flame region. The measured flame temperature profile assuming the particle dispersion exponent is constant at $\alpha = 1$ shows a decrease in flame temperature with increasing distance from the nozzle. The measured decrease in temperature may be an artifact of the constant dispersion exponent assumption. The evolution of soot structure with time is expected to drive evolution in dispersion exponent and this should be considered when extracting the particle temperature.

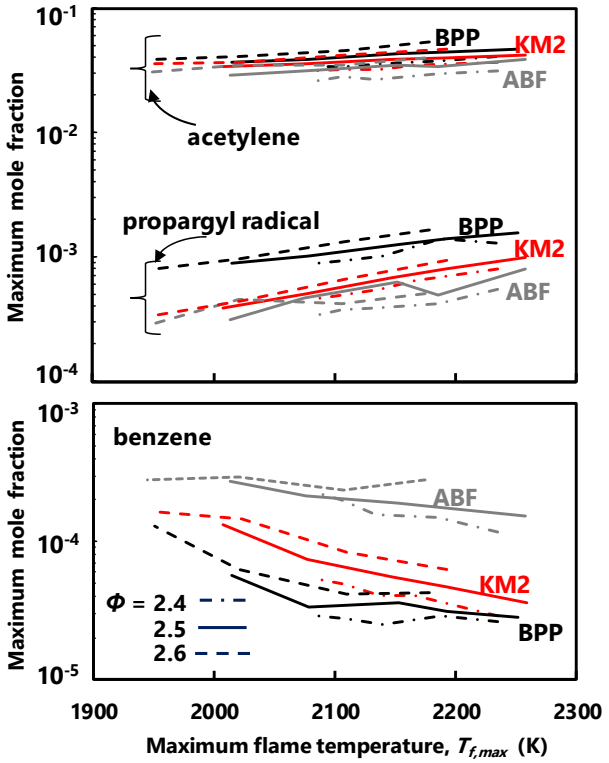

Figure 6: Maximum concentration in computed centerline axial profiles as a function of maximum flame temp-erature. The line follows computations for six flame temperature conditions for each equivalence ratio (see Table 1). Results for each chemistry model (ABF, BPP, KM2) is shown for acetylene and propargyl radical (top) and benzene (bottom).

Using the computed flame temperature as a constraint, a dispersion exponent profile is extracted for the measured grey scale intensity ratios based on eq. 1 and the resulting exponent profiles are shown in Fig. 5. The measured temperature profile based on this fitted dispersion exponent profile is also included in Fig. 4 to demonstrate convergence after applying the computed temperature profile as a constraint. If the computed flame temperature is a reasonable reference point, the fitted profile should fall within physically relevant values. This is indeed the case as the trend and magnitude of the fitted dispersion exponents shown in Fig. 5 could be explained in terms expected soot formation behavior. Namely, the range of values observed ($0.5 < \alpha < 3$) falls with dispersion exponents reported for low C/H organic materials, soot and carbon [57,61,63,64]. Interpretation of radiative emissions from the

flames is subject to experimental uncertainties associated with the camera sensor. This includes error in the Blackbody furnace intensity during calibration, positional errors and errors in the filter properties. For assessment of dispersion coefficient, this also includes uncertainties in the computed flame temperature. A conservative estimated of the error on the measured dispersion coefficient is +/- 5% based on convolution of these errors.

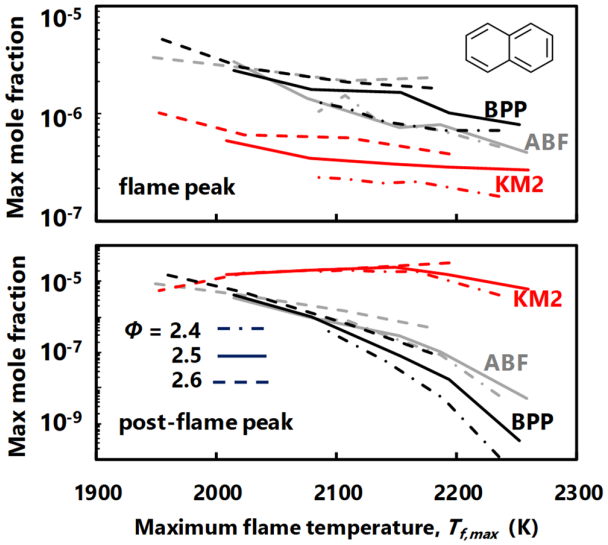

Figure 7: Summary of predicted naphthalene concentrations for the series of flame computations using the three PAH mechanisms. The maximum mole fraction in the computed profile is plotted for each flame taking the maximum at the flame zone (top) and the maximum in the post-flame region (bottom).

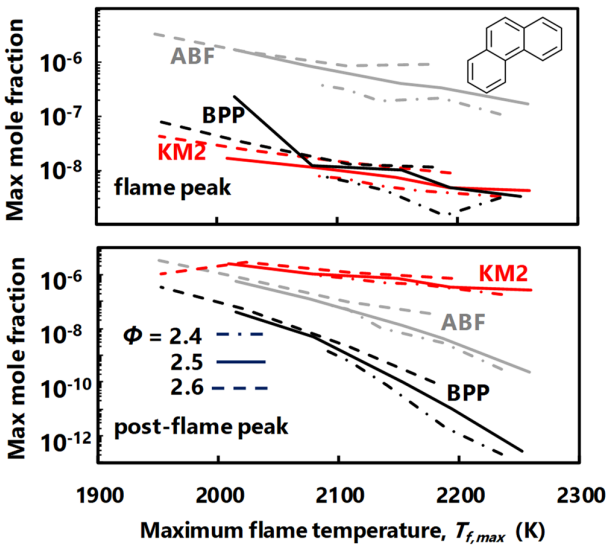

Figure 8: Summary of predicted phenanthrene concentrations for the series of flame computations using the three PAH mechanisms. The maximum mole fraction in the computed profile is plotted for each flame taking the maximum at the flame zone (top) and the maximum in the post-flame region (bottom).

The higher values obtained at the flame-zone correspond to incipient soot which is known to have low C/H structure. The fitted profiles indicate that the dispersion exponent may progress over time towards values on the order of unity corresponding to mature soot. The inset of Fig. 4 shows an example measured temperature field using the fitted axial dispersion exponent profile. A relative trend showing decreasing dispersion exponent for increasing flame temperature and equivalence ratio is also observed across the flames. Color ratio measurements show reasonable agreement to the computed flame position. In addition, constraining the measured particle radiative emissions to match the computed flame temperature results in optical properties consistent with known physical values. The agreement between the measured and computed flame position is assessed by comparing the position of the luminous region with the computed temperature profile. The largest discrepancy occurs for the Φ = 2.4, $T_{f,max}$ = 2190 K case as the measured onset of radiative emissions is approximately 1 mm upstream of the computed pre-heat zone. This upstream shift in position may explain the off-trend dip observed in the dispersion exponent for this case. The expected trend is for the hotter temperature case to have a lower dispersion exponent. This off-trend behavior may be due to artifacts of fitting the temperature profile that does not overlap in space as close as the other cases.

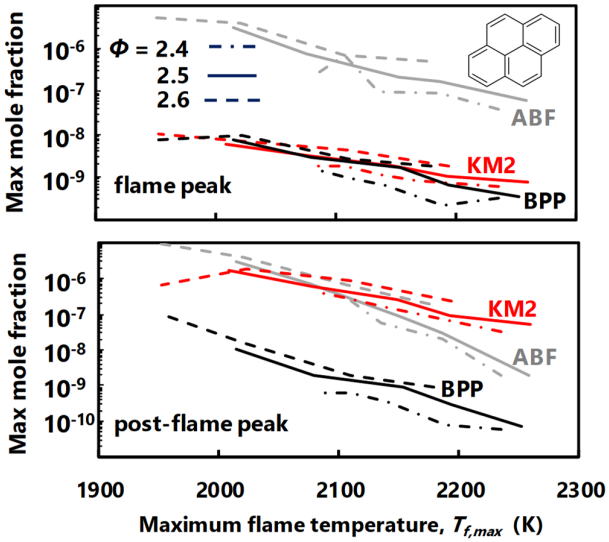

Figure 9: Summary of predicted pyrene concentrations for the series of flame computations using the three PAH mechanisms. The maximum mole fraction in the computed profile is plotted for each flame taking the maximum at the flame zone (top) and the maximum in the post-flame region (bottom).

Having established consistency in the computed flame structure, extrapolation of PAH combustion chemistry models to the higher-temperature regime could be better assessed. Flame structure calculations are carried out for each flame using ABF, BPP and KM2 mechanisms to evaluate the gas-phase environment under which the flame-formed carbon develops. A summary of computed profiles is carried out by determining the maximum mole fraction computed for a species in a certain

flame and designating each flame by the maximum flame temperature. This summary is shown in Fig. 6 for acetylene, propargyl and benzene to establish predictions based on foundational C0-C6 chemistry. As Fig. 6 shows, disagreement in computed concentration is observed among the three PAH chemistry models despite having the same temperature profile constrained by the USC Mech II solution. The computed acetylene concentration increases with equivalence ratio as expected and the predicted trend with flame temperature is relatively similar among the models. In contrast, disagreement among the three models is observed for the predicted concentration of propargyl radical and benzene. The BPP model predicts a significantly higher propargyl radical concentration for the whole range of flame temperature conditions. The predicted species concentration for benzene has a much stronger dependence on the PAH mechanism employed rather than the equivalence ratio. The ABF model predicts benzene concentrations almost an order of magnitude higher than the other models.

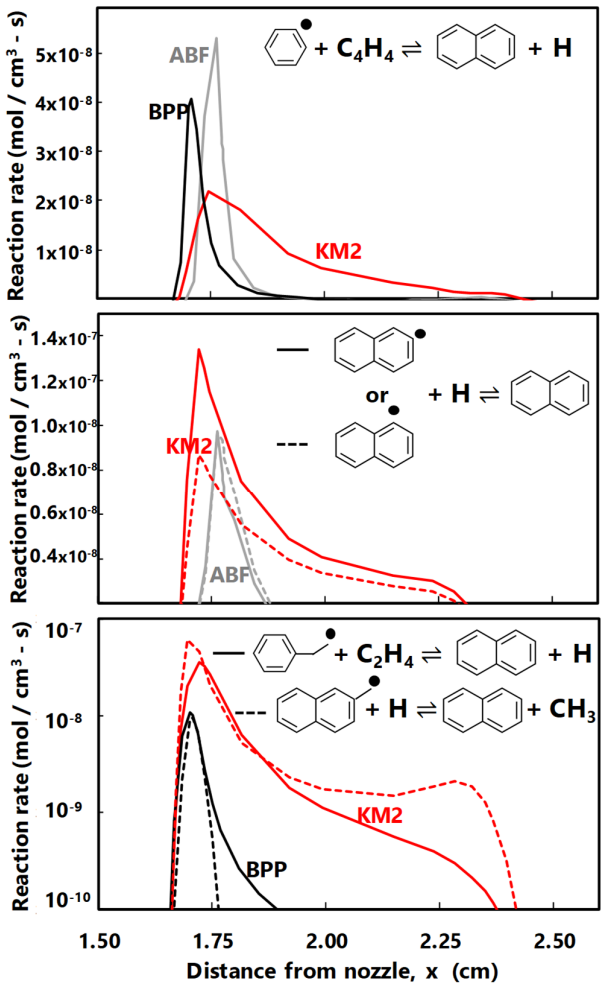

Figure 10: Rate of production of naphthalene predicted from reactions considered in the three PAH mechanisms currently studied including a phenyl based pathway (top), a naphthalene radical based pathway (middle), ethylene substituted benzene pathway (bottom) and methylated naphthalene pathway (bottom).

The observed divergence in computed foundational chemistry is expected to propagate into predictions for larger species. Computed naphthalene, phenanthrene and pyrene profiles for all flames and PAH mechanisms are also included in the supplementary material (Figs. S3-S5). As shown in Fig. 2 and in the supplementary figures, the PAH profiles are non-monotonic as the maximum concentration could occur in the kinetically-driven flame zone or in equilibrium-driven post-flame region. The series of PAH profiles demonstrate the sensitivity of soot precursors to flame temperature and the kinetic mechanism. The profiles of these aromatic soot precursors show peak locations at the flame zone and the post-flame region with relative magnitudes depending on the mechanism employed. The maximum mole fraction computed for naphthalene is shown in Fig. 7 with peak concentration values taken from both the flame zone and the post-flame region. Predicted naphthalene concentrations are more sensitive the kinetic model employed than the equivalence ratio. The BPP and ABF models predict comparable concentrations in the flame zone and post-flame zone for the series of flame temperatures. On the other hand, the KM2 mechanism predicts different behavior in that a relatively low concentration of naphthalene in the flame occurs while more naphthalene is predicted in the post-flame zone. This comparison demonstrates the competing kinetic and thermodynamic processes with regards to PAH chemistry. Ideally, complementary experimental kinetic studies would be employed to constrain the reaction pathways and rate parameters, but this is beyond the current scope.

A summary of PAH predictions is shown in Fig. 8 for phenanthrene formation. The KM2 and BPP predictions for phenanthrene are comparable in the flame zone while the concentration predicted by ABF is an order of magnitude higher. In the post-flame zone, the phenanthrene concentrations span six decades among the three PAH mechanisms. The summary for pyrene concentrations shown in Fig 9 is similar to phenanthrene in that the ABF model predicts an order of magnitude higher concentration in the flame zone. In the post-flame zone, the pyrene concentration predicted by the BPP mechanism is an order of magnitude lower than the other mechanisms. The computed PAH profiles would change with the addition of a soot formation model due to a split between gas-phase and soot-bound carbon depending on particle inception models and kinetic growth rates. PAH chemistry is a notorious bottleneck in quantitative understanding of soot formation and the current analysis demonstrates this challenge for the higher-temperature regime.

The range of PAH profiles predicted among the three PAH mechanisms are due to different pathways and rate parameters adopted. The dominant reactions producing naphthalene are plotted as a function of distance in Fig. 10 for Φ = 2.6, $T_{f,max}$ = 1950 K flame case. This example demonstrates overlaps and divergence in pathways and reaction rates among the three PAH mechanisms. The combination of phenyl and butadienyl to form naphthalene is considered in all three mechanisms but significant discrepancies in rates of production are predicted along the flame profile. Naphthalene production from the naphthalene radical occurs at a comparable rate for the ABF and KM2 models but this is not a dominant pathway for BPP mechanism. Routes to naphthalene from ethylene substituted benzene and methylated naphthalene are dominant only in the

KM2 and BPP mechanisms. The lack of experimental observations of PAH formation in this regime makes assessing chemical reversibility effects and competing mechanism pathways a difficult task. Moreover, application of these PAH mechanisms to soot formation modeling should first consider limitations in PAH chemistry.

With the gas-phase environment established, properties of flame-formed carbon are now assessed. The Raman signature for soot formed in the higher- temperature regime was previously shown to drastically transform from spectra traditionally reported [14]. This was explained in terms of the known response of carbon structures exposed to increasing temperature. In the current work, this approach is expanded to also examine the effect of increasing equivalence ratio. This analysis provides valuable insights into unique higher-temperature soot formation processes and material properties. Raman spectra for primary peaks of deposited films excited with a 532 nm source are shown in Fig. 11 for each flame series. The 5-band deconvolution approach established by Sadezky and co-workers [38] for flame-formed carbon is used to examine known Raman-active modes. Nomenclature of Sadezky is used only for the Raman bands unique to soot (D3 and D4) with the remaining peaks taking labels more commonly reported in the broader carbon literature. As discussed below, D and D' are commonly observed primary bands with corresponding 2D and 2D' secondary bands. Another secondary band is D+G commonly reported at 2945 cm^{-1} for 514.5 nm excitation wavelength. This nomenclature is adopted to compare current observations to other Raman studies of disordered carbon, which unlike soot, show well-defined secondary bands. Baseline correction and deconvolution procedures are described previously [14]. The highest peak intensity is identified in each measured spectrum and this is used to normalize the intensities. The highest peak intensity either appears in the G or D band for the current samples.

For each equivalence ratio series, a striking evolution in the spectra occurs with increasing flame temperature. The series begin with a signature typically reported for soot followed by a drastic shift in relative intensity and peak width. Signatures commonly reported for soot are partially composed of D3 and D4 bands which have been attributed to amorphous components and sp^3 bonds, respectively [38]. Disappearance of the "soot" bands (D3 and D4) with increasing flame temperature may be an indication that material properties of carbon particles formed in the higher-temperature regime differ from soot. Peaks corresponding to the so-called D, G and D' bands also evolve indicating a progression in sp^2 carbon bonding. The G band is attributed to stretching modes of all sp^2 bond pairs. Although highly order graphite only shows a G band, this mode does not require an aromatic ring [39,75–77]. In contrast, the breathing motion of sp^2 bonded carbon in 6-member rings gives rise to the D band and is only observed in lattices deviating from perfect graphite [39,75]. The D' band has been associated with surface sp^2 bonds also in the context of defects to a pristine graphite lattice [38,78].

The width and relative intensity of characteristic Raman bands have been correlated to carbon structural order and crystallinity [39,40,75,79,80]. The ratio of peak intensities for the D and G band (I(D)/I(G)) and the peak widths have been used for quantitative characterization based on phenomenological analysis. The observed evolution in the D and G ratio and peak widths (FWHM) is shown in Fig. 12. At lower flame temperatures, the FWHM of the D peak is much wider than the G peak but significant narrowing of the D peak is observed for the higher temperature conditions. The disappearance of the "soot" bands and significant narrowing of the peaks may indicate that soot formed in the higher-temperature regime approaches the structure reported for other sp^2 carbon materials. Semi-empirical relations developed by Tuinstra and Koenig [79], Ferrari and Robertson [39], Pimenta and co-workers [81], Jorio and co-workers [82] and, more recently, Ferrari [40] have related the relative intensity of the D and G bands to the characteristic size of an uninterrupted sp^2 lattice which, among other labels, has been referred to as the in-plane crystallite size, L_a. Now famous experiments by Jorio and co-workers [82] illustrated the response of Raman scattering to systematic addition of graphene defects by ion bombardment. This work introduced a wide-ranging phenomenological expression for predicting behavior in high and low defect regimes. The so-called defect distance, L_d , was introduced for the ion bombardment experiment to acknowledge that the defect surface density was being measured by Scanning Tunneling Microscopy and this could be related to the length scale of the undisturbed lattice [82].

The phenomenological expression introduced by Jorio and coworkers is applied in the current work for illustrative purposes [82]:

$$\frac{I(D)}{I(G)} = C_A \frac{\left(r_A^2 - r_S^2\right)}{\left(r_A^2 - 2\, r_S^2\right)} \left(exp\left(\frac{-\pi\, r_S^2}{L_D^2}\right) - exp\left(\frac{-\pi\,\left(r_A^2 - r_S^2\right)}{L_D^2}\right)\right) + C_S \left(1 - exp\left(\frac{-\pi\, r_S^2}{L_D^2}\right)\right) \quad \text{eq. 2}$$

where I(D) / I(G) is the relative intensity of the D and G peaks in the Raman spectrum and the rest of the parameters are established based on the ion bombardment experiment on graphene. The defect induced by bombardment of Ar+ creates a "structurally disordered" area with radius r_S. A larger area also surrounds the defect with radius r_A having a mixture states due to proximity to the defect. The coefficient c_A has been characterized as a measure of the maximum I(D)/I(G) ratio with a theoretical limit tied to electron-phonon coupling [82]. The c_S coefficient is related to the I(D)/I(G) ratio in the highly disorder limit. Parameter values from the ion bombardment experiments are adopted (r_A = 3.0 nm, r_S = 1.0 nm, c_A = 4.6 , c_S = 0.87) to extract the defect distance, L_D , of our flame-formed carbon. Although the parameters may not precisely correspond to the current flame formed carbon, the above expression may shed light on the evolution in carbon structure with increasing flame temperature. In fact, the narrow bands, prominent D' band and evolution of the current Raman spectra are features shared with reported spectra for studies on evolution of disorder for multi-layer graphene [82–84].

The classical formulation relating L_a to I(D)/I(G) postulated by Tuinstra and Koenig [79] has been predicted to be limited for applications to graphitic materials with L_a > 3 nm [39,40,81,82]. Using this limit to separate high and low disordered regimes, Ferrari introduced semi-empirical relations to correlate the defect distance to intensity ratio and the excitation energy with separate equations for the high and low-defects [40]. Raman

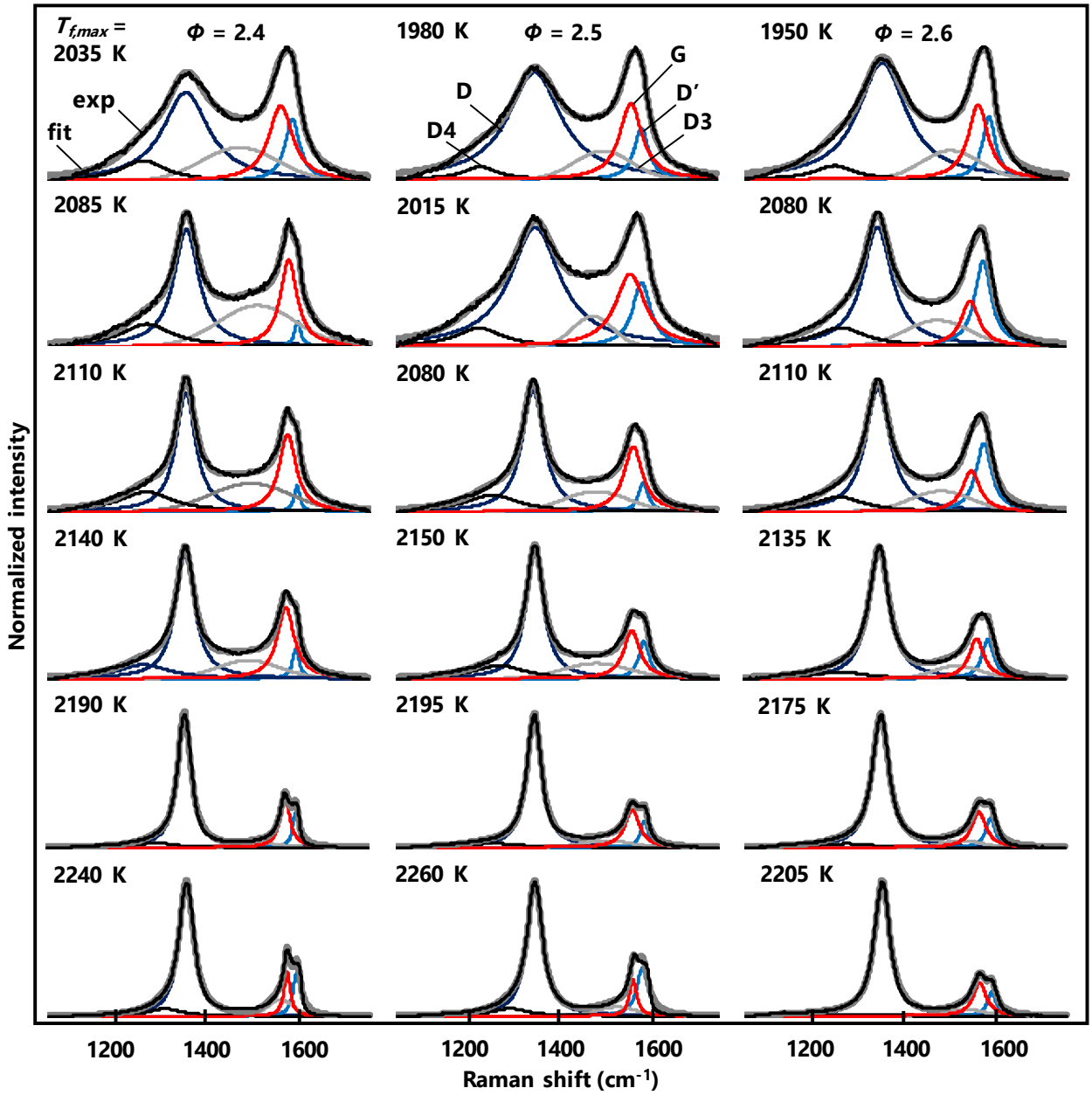

Figure 11 Baseline-corrected Raman spectra of primary peaks for all flame conditions (532 nm excitation source). The measured spectra are fitted according to the five-band deconvolution.

spectra of the current flame-formed carbon may correspond to the high-defect density regime reported in several systematic studies where the I(D) / I(G) ratio was shown to increase with the defect distance [39,40,76,77,80]. The expression given in the context of high defect graphene by Ferrari and Basko [40], is used in the current work as a second method to correlate to the defect distance for the flame-formed carbon currently investigated. The following is applied for the regime in which L_D < 3 nm:

$$L_D^2 = 5.4 \times 10^{-2}\, E_L^4 \frac{I(D)}{I(G)} \qquad \text{eq. 3}$$

where E_L is the excitation energy in electron volts. The excitation energy is E_L = 2.33 eV corresponding to the 532 nm excitation source used in this work. The dependence on excitation energy in eq. 3 is also based on ion bombardment experiments [84] and the empirical expression c_A = (160 ± 48 eV^4) E_L^{-4} is embedded to account for dispersion effects observed in the bombardment experiments.

The evolution in defect distance computed from the above expressions is shown in Fig. 13 for the series of flame temperatures currently studied. A defect distance on the order of unity observed for the lower flame temperatures is in agreement with reports for typical flame soot. Miller and co-workers have interpreted this size to correspond to a building

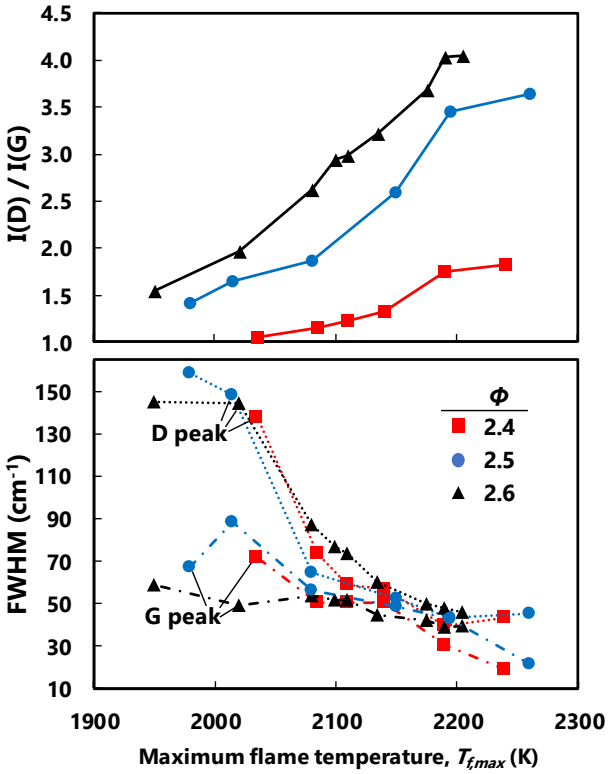

Figure 12: Evolution in I(D)/I(G) (top) and peak FWHM (bottom) based on Raman spectra of deposited carbon films for all flame conditions studied. Lines are drawn to guide the eye.

block of soot on the order of 4-5 aromatic rings [25]. For all equivalence ratio conditions, the observed defect distance increases with increasing flame temperature. This trend is in line with known carbon annealing behavior [76,85] and entropy-driven carbonization processes [86,87]. In addition, a systematic trend is observed showing, for a given flame temperature, the defect distance increases with equivalence ratio. That is, a larger region of crystalline carbon structure is observed with higher equivalence ratio. Development of a mechanistic description of this trend is beyond the current scope but this observation may be explained on the basis of carbon lattice defects. Namely, the greater abundance of gas-phase PAH surrounding the carbon may facilitate development or "healing" of an ordered lattice during formation and growth.

The I(D)/I(G) ratio measured for the current flame-formed carbon is higher than the peak ratio of ~3.5 reported by Jorio and co-workers [82] and this may be due to the slightly different excitation energy applied or carbon structural differences. As such, the Jorio expression does not converge for the Φ = 2.5 and 2.6 cases above 2150 K due to the relatively high I(D)/I(G). A third expression is applied here which combines the original Jorio expression with the excitation energy dependence. The 2.33 eV excitation applied in the current measurements corresponds to of c_A = 5.4 according to the $c_A(E_L)$ correlation embedded in eq. 3 [84]. The predictions based on the Jorio expression incorporating this modified parameter is also included here. As Fig. 13 shows, there is up to a 30% discrepancy observed between the three defect distance predictions. These correlations were developed for graphene materials and specifically calibrated for separate ion bombardment experiments. As such, application to the current flame-formed carbon is an extrapolation of these correlations and disagreement among the predictions is expected. Nonetheless, the qualitative trends of increasing order with increasing temperature and equivalence ratio still hold despite limitations of the current assumptions. Although, the parameters and correlations are borrowed from bombardment studies on graphene materials, the trends predicted for the current flame-formed carbon are informative. Typical Raman spectra reported for soot show mild changes for studies done at typical flame temperatures. In contrast, the response of the Raman spectra of flame-formed carbon to higher-temperature conditions is dramatic and this can be interpreted to indicate that the carbon structure is more ordered than typical soot.

Secondary bands are not typically analyzed for soot formed at conventional flame temperature because soot is relatively disordered. In contrast, Raman spectra from the current high-temperature carbon products show distinct secondary bands. The evolution in secondary peaks is shown in Fig. 14 for all flame conditions studied. Secondary peaks corresponding to

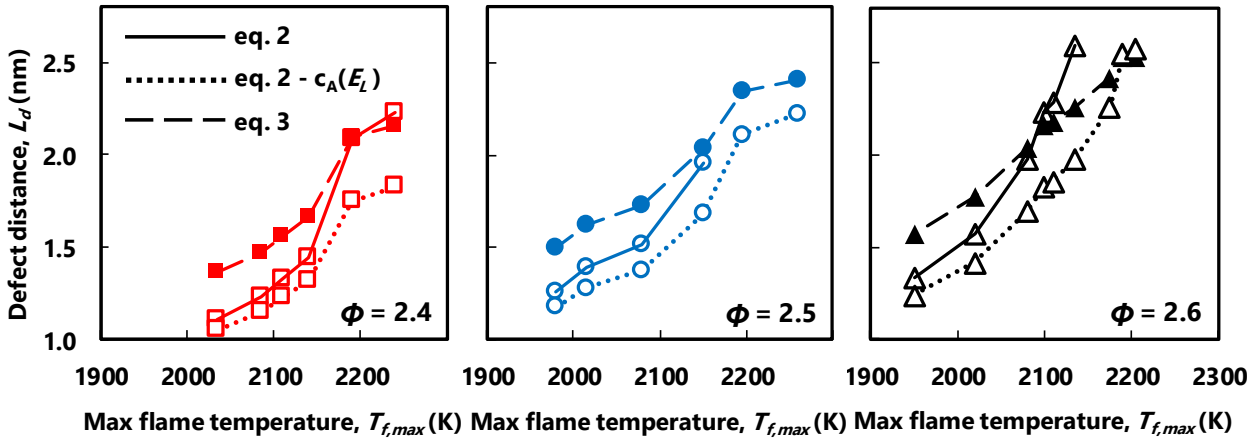

Figure 13 Evolution in defect distance based on Raman spectra of deposited carbon films for all flame conditions studied. The Φ = 2.4 (left), Φ = 2.5 (middle) and Φ = 2.6 (right) predictions are shown for three different correlations. The lines are drawn to guide the eye.

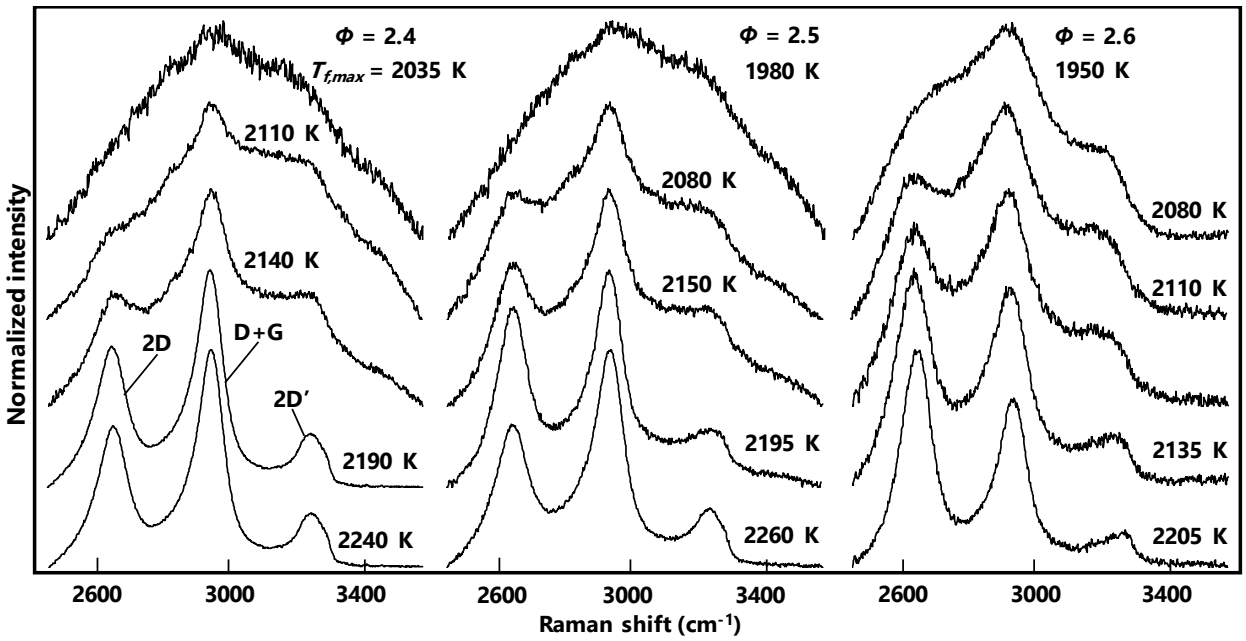

Figure 14 Evolution in baseline-corrected secondary Raman peaks for all flame conditions studied.

overtones of the D, G and D' bands are discernable for carbon formed at flame temperature hotter than 2050 K. In literature for disordered sp^2 carbon materials, these are bands are denoted as 2D and 2D' with an additional secondary band denoted as D+G. The secondary peaks become narrower and more resolved as flame temperature is increased. Interestingly, the 2D band is commonly considered to be the most prominent peak in the secondary spectra of disordered carbon [76,88] but the D+G band is only dominant for the middle range of flame temperatures currently studied. The observed evolution in Raman signature may indicate the current flame-formed carbon transitions from conventional soot to structure observed in high-defect sp^2 carbon.

The higher equivalence ratio series shows the most resolved secondary peaks in accord with the relative evolution of the primary peaks. Deconvolution of the 2D band into $2D_1$ and $2D_2$ bands is carried out as established in literature for disordered graphite an graphene materials [77,88]. Deconvolution for the highest temperature conditions of the Φ = 2.6 case is shown in Fig. 15 with results for Φ = 2.4 and 2.5 cases shown in supplementary material. A transition occurs whereby the $2D_1$ is greatest at the 2110 K flame condition and becomes usurped by the $2D_2$ peak at higher flame temperature. These relative intensities has been reported as a transition from powdered graphite to a carbon structure approaching highly ordered pyrolytic graphite [88]. Analysis on flame-formed carbon nano-discs reported by D'Anna and co-workers [89] provides an additional example of a unique structure having features of both stacked graphitic carbons and three-dimensional turbostratic structures. The secondary peaks observed in the intermediate temperature range of the current work may correspond to the aforementioned features of the nano-disc Raman spectra followed by evolution to more ordered structure with increasing temperature. The Raman-active modes of carbon enable the subtle variation in carbon structure to be examined for the series of flame conditions currently studied. The Raman spectra provide evidence that carbon structure approaching sp^2 carbon materials could be obtained. This is especially promising if the precise carbon structure could be functionalized for tuned material behavior.

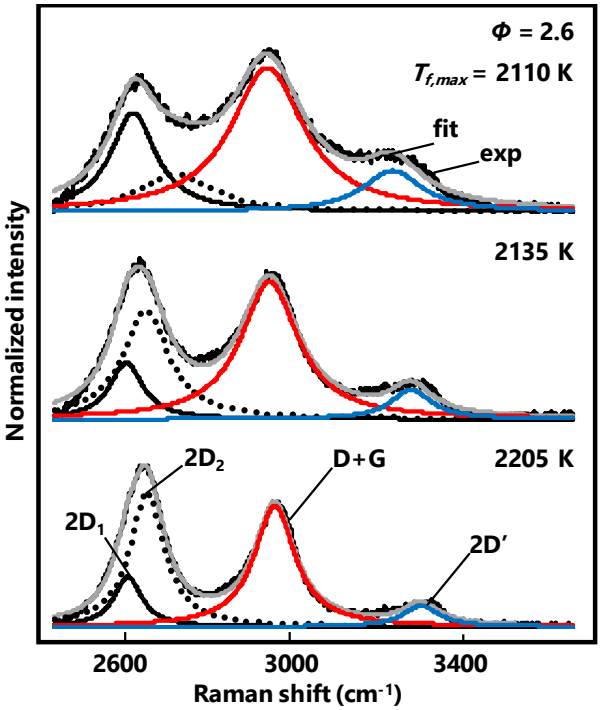

Figure 15: Baseline-corrected deconvoluted Raman peaks (2D band) for the Φ = 2. 6 case with increasing flame temperature.

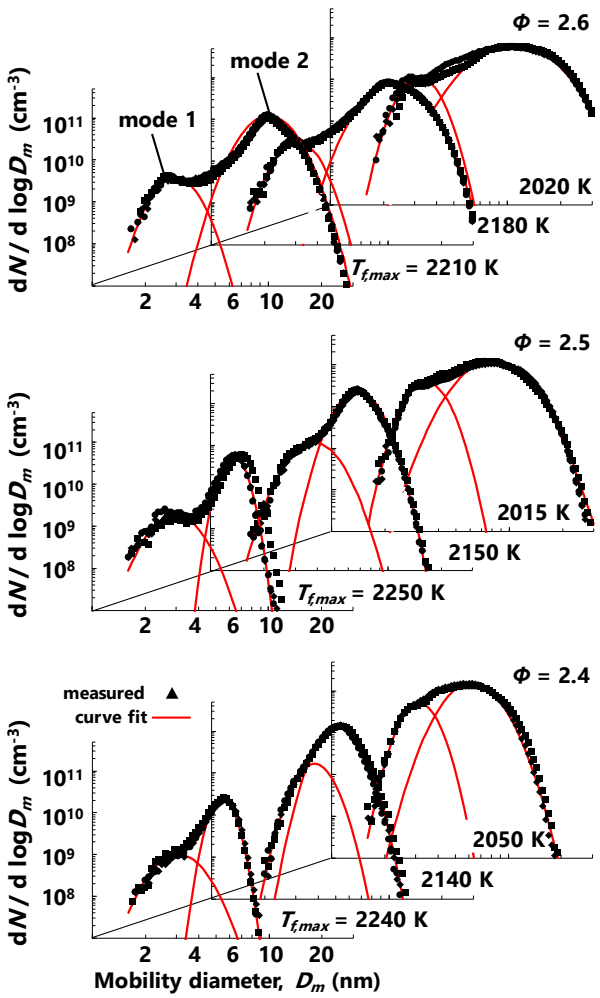

Figure 16: Measured PSDF for selected flame conditions. Symbols are measurements and lines are curve fits to a lognormal distribution for each size mode.

Direct observations of unique higher-temperature soot formation processes are also reported here in terms of detailed PSDF measured by mobility particle sizing. An established aerosol sampling method [13,47] is applied to quantitatively follow evolution in the size distribution for increasing flame temperature and equivalence ratio. Measured PSDF for each flame series is shown in Fig. 16 along with lognormal curve fits of the observed bimodal distribution. The observed decrease in number and size range with increasing flame temperature for each equivalence ratio series is expected based on reversibility in precursor formation and reduced collision efficiency. A bimodal distribution consisting of nucleation-sized particles and a slightly larger mode of growth particles is observed in all cases. For the highest temperature cases, a visible split between the size modes becomes apparent as the width of the growth mode significantly narrows. PSDF in premixed sooting flames at conventional flame temperature (see e.g [11,12]) have reported a bimodal distribution with a dominant nucleation mode relative to the growth mode. The magnitude of the nucleation mode is lower in the PSDF currently observed which may indicate that nucleation processes are not as persistent in the higher-temperature soot formation regime.

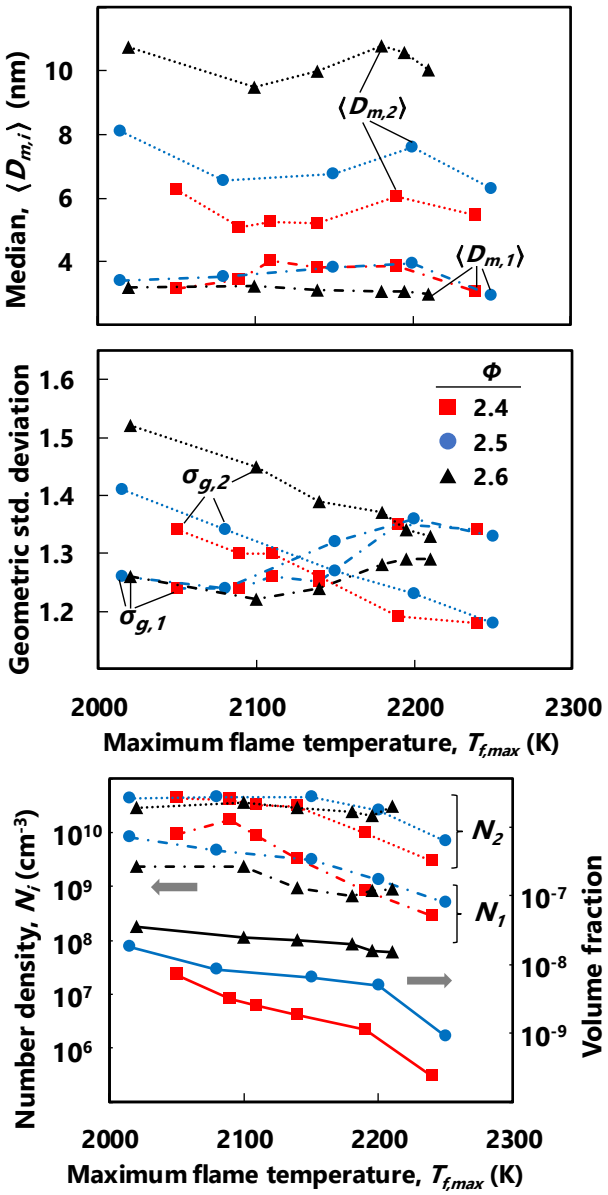

Figure 17: Global properties determined from log-normal curve fits of the bimodal PSDF including median diameter (top), geometric standard deviation (middle), number density and PSDF volume fraction (bottom).

Parameters of the log-normal curve fitting provide further insight into competing soot formation processes in terms of global properties of the size distribution. The global parameters are plotted for each maximum flame temperature condition in Fig. 17. The median diameter of the growth mode varies by nearly a factor of two between the lowest and highest equivalence ratio cases. In contrast, the nucleation-size mode has a median of 3 nm across all conditions. The observed size range corresponds to isolated primary particles and small particle clusters rather than larger aggregates. Evolution in the geometric standard deviation occurs in opposing directions for the two size modes which may indicate size-dependent particle growth processes are occurring. The number density is nearly an order of magnitude greater for the growth mode particles

and reduction in soot yield with increasing flame temperature is observed in terms of number density and volume fraction. These measurements indicate that ultra-fine carbon nanoparticles with relatively narrow size distribution is produced for the flame conditions studied. The observed evolution in size distribution and carbon structure provides insight for soot formation modeling in the higher-temperature regime. Moreover, the observed transition from soot to structure corresponding to disordered sp^2 carbon may be promising for functional high-surface area carbon materials. Relatively high flame temperatures explored here enable soot produced with unique characteristics. The ultrafine particle size characteristic to incipient soot is combined with a carbon structure more ordered than that of mature soot. Functional material properties arising from this unique structure to be explored in the future include electrical conductivity and electrochemical behavior.

4. Conclusions

A complementary experimental and modeling study is reported to shed light on formation processes and material properties for soot formed in the higher-temperature regime (T_f > 2100 K). The effects of flame temperature and equivalence ratio are isolated in a series of premixed stretch-stabilized flames. Flame structure computations show reasonable agreement to measured color-ratio intensity profiles in terms of the flame position and interpretation of the particle optical dispersion exponent. Computations using KM2, ABF and BPP combustion chemistry models show that predictions of PAH concentration profiles for the current higher-temperature flames are more sensitive to the choice in mechanism rather than specific flame conditions.

As for material properties, the Raman signatures transition from a typical soot spectrum to features observed in disordered sp^2 carbon materials. This is inferred from the disappearance of D3 and D4 bands and significant narrowing of all Raman peaks. Shift in the relative intensity of D and G bands and increased definition of the corresponding overtones are another indication that the structure is more ordered than typical soot. A shift in relative intensity of the $2D_1$ and $2D_2$ secondary bands is observed which tends towards increasing carbon structural order. The defect distance extracted from the Raman spectra begins on the order of unity for flame temperatures close to conventional flame studies and nearly doubles as the flame temperature exceeds 2200 K. Higher concentrations of gas-phase precursors may facilitate development of an ordered carbon structure as indicated by the relatively high defect distance observed for the highest equivalence ratio series.

Measured particle size distributions provide further insight into unique soot formation processes in the higher-temperature regime. As expected, the size and yield of soot decreases with increasing flame temperature due to expected reduction in precursor formation and collision efficiency. The observed ultra-fine size range is also expected, even for the larger growth mode of the bimodal distribution. Unlike PSDF reported for conventional flame temperature conditions, the mode of nucleation-sized particles does not dominate in the higher-temperature regime. In addition, the median diameter for the nucleation mode is close to 4 nm for all flame conditions while the growth mode for the higher equivalence ratio cases have significantly larger median diameters. Systematic observation of size distribution and carbon structure provides a sound basis for developing soot formation models in the higher-temperature regime. This is especially promising if the significant transformation in carbon structure inferred from the evolution in Raman spectra enables development of functional high-surface area sp^2 carbon materials.

Conflicts of interest

There are no conflicts to declare

Acknowledgements

The work was supported by NSF Combustion and Fire Systems program under Award 1841357. Prof. David Pullman (SDSU Chemistry) and Dr. Ingrid Neisman (SDSU Microscopy Center) are gratefully acknowledged for assistance in nanoparticle characterization.

References

[1] J.B. Heywood, Internal Combustion Engine Fundamentals, McGraw-Hill, New York, 2018.

[2] I.M. Kennedy, The health effects of combustion-generated aerosols, Proc. Combust. Inst. 31 (2007) 2757–2770. https://doi.org/https://doi.org/10.1016/j.proci.2006.08.116.

[3] M.C. Jacobson, H.C. Hansson, K.J. Noone, R.J. Charlson, Organic atmospheric aerosols: Review and state of the science, Rev. Geophys. 38 (2000) 267–294. https://doi.org/10.1029/1998RG000045.

[4] G.D. Ulrich, Special Report: Flame-generated fine particles, Chem. Eng. News Arch. 62 (1984) 22–29. https://doi.org/10.1021/cen-v062n032.p022.

[5] J.-B. Donnet, R.C. Bansal, M.-J. Wang, Carbon Black, Marcel Dekker, New York, 1993.

[6] T.-S. Wang, Thermophysics Characterization of Kerosene Combustion, J. Thermophys. Heat Transf. 15 (2001) 140–147. https://doi.org/10.2514/2.6602.

[7] T. Ochs, D. Oryshchyn, R. Woodside, C. Summers, B. Patrick, D. Gross, M. Schoenfield, T. Weber, D. O'Brien, Results of initial operation of the Jupiter Oxygen Corporation oxy- fuel 15 MWth burner test facility, Energy Procedia. 1 (2009) 511–518. https://doi.org/https://doi.org/10.1016/j.egypro.2009.01.068.

[8] C.R. Shaddix, T.C. Williams, The effect of oxygen enrichment on soot formation and thermal radiation in turbulent, non-premixed methane flames, Proc. Combust. Inst. 36 (2017) 4051–4059. https://doi.org/https://doi.org/10.1016/j.proci.2016.06.106.

[9] M. Frenklach, S. Taki, M.B. Durgaprasad, R.A. Matula, Soot formation in shock-tube pyrolysis of acetylene, allene, and 1,3-butadiene, Combust. Flame. 54 (1983) 81–101. https://doi.org/https://doi.org/10.1016/0010-2180(83)90024-X.

[10] H. Böhm, D. Hesse, H. Jander, B. Lüers, J. Pietscher, H.G.G. Wagner, M. Weiss, The influence of pressure and temperature on soot formation in premixed flames, Symp. Combust. 22 (1989) 403–411. https://doi.org/https://doi.org/10.1016/S0082-0784(89)80047-5.

[11] A.D. Abid, N. Heinz, E.D. Tolmachoff, D.J. Phares, C.S. Campbell, H. Wang, On evolution of particle size distribution functions of incipient soot in premixed ethylene–oxygen–argon flames, Combust. Flame. 154 (2008) 775–788. https://doi.org/https://doi.org/10.1016/j.combustflame.2008.06.009.

[12] C. Gu, H. Lin, J. Camacho, B. Lin, C. Shao, R. Li, H. Gu, B. Guan, Z. Huang, H. Wang, Particle size distribution of nascent soot in lightly and heavily sooting premixed ethylene flames, Combust. Flame. 165 (2016) 177–187. https://doi.org/10.1016/j.combustflame.2015.12.002.

[13] J. Camacho, A. V. Singh, W. Wang, R. Shan, E.K.Y. Yapp, D. Chen, M. Kraft, H. Wang, Soot particle size distributions in premixed stretch-stabilized flat ethylene-oxygen-argon flames, Proc. Combust. Inst. 36 (2017) 1001–1009. https://doi.org/10.1016/j.proci.2016.06.170.

[14] J. Bonpua, Y. Yagües, A. Aleshin, S. Dasappa, J. Camacho, Flame temperature effect on sp2 bonds on nascent carbon nanoparticles formed in premixed flames (T > 2100 K): A Raman spectroscopy and particle mobility sizing study, Proc. Combust. Inst. 37 (2019) 943–951. https://doi.org/10.1016/j.proci.2018.06.124.

[15] E. Meeks, R.J. Kee, D.S. Dandy, M.E. Coltrin, Computational simulation of diamond chemical vapor deposition in premixed C2H2/O2/H2 and CH4O2-strained flames, Combust. Flame. 92 (1993) 144–160. https://doi.org/http://dx.doi.org/10.1016/0010-2180(93)90204-G.

[16] M. Frenklach, D.W. Clary, W.C. Gardiner, S.E. Stein, Detailed kinetic modeling of soot formation in shock-tube pyrolysis of acetylene, Symp. Combust. 20 (1985) 887–901. https://doi.org/https://doi.org/10.1016/S0082-0784(85)80578-6.

[17] H. Wang, Formation of nascent soot and other condensed-phase materials in flames, Proc. Combust. Inst. 33 (2011) 41–67. https://doi.org/http://dx.doi.org/10.1016/j.proci.2010.09.009.

[18] A. D'Alessio, A.C. Barone, R. Cau, A. D'Anna, P. Minutolo, Surface deposition and coagulation efficiency of combustion generated nanoparticles in the size range from 1 to 10nm, Proc. Combust. Inst. 30 (2005) 2595–2603. https://doi.org/https://doi.org/10.1016/j.proci.2004.08.267.

[19] W. Pejpichestakul, A. Frassoldati, A. Parente, T. Faravelli, Kinetic modeling of soot formation in premixed burner-stabilized stagnation ethylene flames at heavily sooting condition, Fuel. 234 (2018) 199–206. https://doi.org/https://doi.org/10.1016/j.fuel.2018.07.022.

[20] M.R. Kholghy, A. Veshkini, M.J. Thomson, The core–shell internal nanostructure of soot – A criterion to model soot maturity, Carbon N. Y. 100 (2016) 508–536. https://doi.org/https://doi.org/10.1016/j.carbon.2016.01.022.

[21] K.O. Johansson, F. El Gabaly, P.E. Schrader, M.F. Campbell, H.A. Michelsen, Evolution of maturity levels of the particle surface and bulk during soot growth and oxidation in a flame, Aerosol Sci. Technol. 51 (2017) 1333–1344. https://doi.org/10.1080/02786826.2017.1355047.

[22] R.A. Dobbins, Soot inception temperature and the carbonization rate of precursor particles, Combust. Flame. 130 (2002) 204–214. https://doi.org/http://dx.doi.org/10.1016/S0010-2180(02)00374-7.

[23] R. Dastanpour, A. Momenimovahed, K. Thomson, J. Olfert, S. Rogak, Variation of the optical properties of soot as a function of particle mass, Carbon N. Y. 124 (2017) 201–211. https://doi.org/https://doi.org/10.1016/j.carbon.2017.07.005.

[24] C. Russo, B. Apicella, J.S. Lighty, A. Ciajolo, A. Tregrossi, Optical properties of organic carbon and soot produced in an inverse diffusion flame, Carbon N. Y. 124 (2017) 372–379. https://doi.org/https://doi.org/10.1016/j.carbon.2017.08.073.

[25] J.D. Herdman, B.C. Connelly, M.D. Smooke, M.B. Long, J.H. Miller, A comparison of Raman signatures and laser-induced incandescence with direct numerical simulation of soot growth in non-premixed ethylene/air flames, Carbon N. Y. 49 (2011) 5298–5311. https://doi.org/https://doi.org/10.1016/j.carbon.2011.07.050.

[26] M. Commodo, G. De Falco, A. Bruno, C. Borriello, P. Minutolo, A. D'Anna, Physicochemical evolution of nascent soot particles in a laminar premixed flame: from nucleation to early growth, Combust. Flame. 162 (2015) 3854–3863. https://doi.org/https://doi.org/10.1016/j.combustflame.2015.07.022.

[27] M. Commodo, G. Tessitore, G. De Falco, A. Bruno, P. Minutolo, A. D'Anna, Further details on particle inception and growth in premixed flames, Proc. Combust. Inst. 35 (2015) 1795–1802. https://doi.org/https://doi.org/10.1016/j.proci.2014.06.004.

[28] M. Sirignano, A. Ciajolo, A. D'Anna, C. Russo, Chemical Features of Particles Generated in an Ethylene/Ethanol Premixed Flame, Energy & Fuels. 31 (2017) 2370–2377. https://doi.org/10.1021/acs.energyfuels.6b02372.

[29] C. Russo, A. D'Anna, A. Ciajolo, M. Sirignano, Analysis of the chemical features of particles generated from ethylene and ethylene/2,5 dimethyl furan flames, Combust. Flame. 167 (2016) 268–273. https://doi.org/https://doi.org/10.1016/j.combustflame.2016.02.003.

[30] M. Sirignano, D. Bartos, M. Conturso, M. Dunn, A. D'Anna, A. R. Masri, Detection of nanostructures and soot in laminar premixed flames, Combust. Flame. 176 (2017) 299–308. https://doi.org/10.1016/j.combustflame.2016.10.009.

[31] F. Picca, G. De Falco, M. Commodo, G. Vitiello, G. D'Errico, P. Minutolo, A. D'Anna, Characteristics of Flame-nucleated Carbonaceous Nanoparticles, Chem. Eng. Trans. 73 (2019) 61-66 SE-Research Articles. https://doi.org/10.3303/CET1973011.

[32] M. Commodo, G. De Falco, P. Minutolo, A. D'Anna, Structure and size of soot nanoparticles in laminar premixed flames at different equivalence ratios, Fuel. 216 (2018) 456–462. https://doi.org/https://doi.org/10.1016/j.fuel.2017.12.032.

[33] M. Commodo, P.H. Joo, G. De Falco, P. Minutolo, A. D'Anna, Ö.L. Gülder, Raman Spectroscopy of Soot Sampled in High-Pressure Diffusion Flames, Energy & Fuels. 31 (2017) 10158–10164. https://doi.org/10.1021/acs.energyfuels.7b01674.

[34] K. Hayashida, Y. Miki, Analysis of Graphitic Crystallites Evolution of Soot Particles in a Diffusion Flame, BUNSEKI KAGAKU. 66 (2017) 343–350. https://doi.org/10.2116/bunsekikagaku.66.343.

[35] K. Hayashida, S. Nagaoka, H. Ishitani, Growth and oxidation of graphitic crystallites in soot particles within a laminar diffusion flame, Fuel. 128 (2014) 148–154. https://doi.org/https://doi.org/10.1016/j.fuel.2014.03.008.

[36] M. Commodo, A.E. Karataş, G. De Falco, P. Minutolo, A. D'Anna, Ö.L. Gülder, On the effect of pressure on soot nanostructure: A Raman spectroscopy investigation, Combust. Flame. 219 (2020) 13–19. https://doi.org/https://doi.org/10.1016/j.combustflame.2020.04.008.

[37] M. Saffaripour, L.-L. Tay, K.A. Thomson, G.J. Smallwood, B.T. Brem, L. Durdina, M. Johnson, Raman spectroscopy and TEM characterization of solid particulate matter emitted from soot generators and aircraft turbine engines, Aerosol Sci. Technol. 51 (2017) 518–531. https://doi.org/10.1080/02786826.2016.1274368.

[38] A. Sadezky, H. Muckenhuber, H. Grothe, R. Niessner, U. Poschl, Raman microspectroscopy of soot and related carbonaceous materials: Spectral analysis and structural information, Carbon 43 (2005) 1731–1742. https://doi.org/http://dx.doi.org/10.1016/j.carbon.2005.02.018.

[39] A.C. Ferrari, J. Robertson, Interpretation of Raman spectra of disordered and amorphous carbon, Phys. Rev. B. 61 (2000) 14095–14107. http://link.aps.org/doi/10.1103/PhysRevB.61.14095.

[40] A.C. Ferrari, D.M. Basko, Raman spectroscopy as a versatile tool for studying the properties of graphene, Nat. Nanotechnol. 8 (2013) 235. https://doi.org/10.1038/nnano.2013.46https://www.nature.com/articles/nnano.2013.46#supplementary-information.

[41] C.K. Law, Combustion Physics, Cambrige Press, Cambridge, 2006.

[42] A.E. Lutz, R.J. Kee, J.F. Grcar, F.M. Rupley, OPPDIF: A Fortan program for computing opposed-flow diffusion flames, (1997).

[43] T. Von Karman, On laminar and turbulent friction, NACA Tech. Memo. (1921) 1092.

[44] K. Seshadri, F.A. Williams, Laminar flow between parallel plates with injection of a reactant at high reynolds number, Int. J. Heat Mass Transf. 21 (1978) 251–253. https://doi.org/https://doi.org/10.1016/0017-9310(78)90230-2.

[45] V. Giovangigli, M.D. Smooke, Extinction of Strained Premixed Laminar Flames With Complex Chemistry, Combust. Sci. Technol. 53 (1987) 23–49. https://doi.org/10.1080/00102208708947017.

[46] S. Dasappa, J. Camacho, Formation of nanocrystalline manganese oxide in flames: oxide phase governed by classical nucleation and size-dependent equilibria, CrystEngComm. 22 (2020) 5509–5521. https://doi.org/10.1039/D0CE00734J.

[47] A.D. Abid, J. Camacho, D.A. Sheen, H. Wang, Quantitative measurement of soot particle size distribution in premixed flames - The burner-stabilized stagnation flame approach, Combust. Flame. 156 (2009) 1862–1870.

[48] H. Wang, X. You, A. V Joshi, S.G. Davis, A. Laskin, F. Egolfopoulos, C.K. Law, USC Mech II. High-Temperature Combustion Reaction Model of H2/CO/C1-C4 Compounds, Http://Ignis.Usc.Edu/USC_Mech_II.Htm. (2007).

[49] A. Raj, I.D.C. Prada, A.A. Amer, S.H. Chung, A reaction mechanism for gasoline surrogate fuels for large polycyclic aromatic hydrocarbons, Combust. Flame. 159 (2012) 500–515. https://doi.org/https://doi.org/10.1016/j.combustflame.2011.08.011.

[50] J. Appel, H. Bockhorn, M. Frenklach, Kinetic modeling of soot formation with detailed chemistry and physics: laminar premixed flames of C2 hydrocarbons, Combust. Flame. 121 (2000) 122–136. https://doi.org/https://doi.org/10.1016/S0010-2180(99)00135-2.

[51] G. Blanquart, P. Pepiot-Desjardins, H. Pitsch, Chemical mechanism for high temperature combustion of engine relevant fuels with emphasis on soot precursors, Combust. Flame. 156 (2009) 588–607. https://doi.org/https://doi.org/10.1016/j.combustflame.2008.12.007.

[52] Y. Wang, A. Raj, S.H. Chung, A PAH growth mechanism and synergistic effect on PAH formation in counterflow diffusion flames, Combust. Flame. 160 (2013) 1667–1676. https://doi.org/https://doi.org/10.1016/j.combustflame.2013.03.013.

[53] G.P. Smith, D.M.. Golden, M. Frenklach, N.W.. Moriarty, B. Eiteneer, M. Goldenberg, C.T. Bowman, R.K. Hanson, S. Song, W.C.. Gardiner, V.V.. Lissianski, Z. Qin, GRI-Mech 3.0, Http://Www.Me.Berkeley.Edu/Gri_mech/. (n.d.).

[54] J. Camacho, C. Liu, C. Gu, H. Lin, Z. Huang, Q. Tang, X. You, C. Saggese, Y. Li, H. Jung, L. Deng, I. Wlokas, H. Wang, Mobility size and mass of nascent soot particles in a benchmark premixed ethylene flame, Combust. Flame. 162 (2015). https://doi.org/10.1016/j.combustflame.2015.07.018.

[55] TSI, Diffusion correction using TSI's 1 nm SMPS SYSTEM Model 3938, Application note SMPS-010 (US), 2019.

[56] Z. Li, H. Wang, Drag force, diffusion coefficient, and electric mobility of small particles. II. Application, Phys. Rev. E. 68 (2003) 61207. https://link.aps.org/doi/10.1103/PhysRevE.68.061207.

[57] H. Guo, J.A. Castillo, P.B. Sunderland, Digital camera measurements of soot temperature and soot volume fraction in axisymmetric flames, Appl. Opt. 52 (2013) 8040–8047. https://doi.org/10.1364/AO.52.008040.

[58] K. Gleason, F. Carbone, A. Gomez, Effect of temperature on soot inception in highly controlled counterflow ethylene diffusion flames, Combust. Flame. 192 (2018) 283–294. https://doi.org/https://doi.org/10.1016/j.combustflame.2018.02.001.

[59] F. Xu, P.B. Sunderland, G.M. Faeth, Soot formation in laminar premixed ethylene/air flames at atmospheric pressure, Combust. Flame. 108 (1997) 471–493. https://doi.org/http://dx.doi.org/10.1016/S0010-2180(96)00200-3.

[60] Y. Matsui, T. Kamimoto, S. Matsuoka, A Study on the Time and Space Resolved Measurement of Flame Temperature and Soot Concentration in a D.I. Diesel Engine by the Two-Color Method, SAE Trans. 88 (1979) 1808–1822. http://www.jstor.org/stable/44658183.

[61] F. Carbone, S. Moslih, A. Gomez, Probing gas-to-particle transition in a moderately sooting atmospheric pressure ethylene/air laminar premixed flame. Part II: Molecular clusters and nascent soot particle size distributions, Combust. Flame. 181 (2017) 329–341. https://doi.org/https://doi.org/10.1016/j.combustflame.2017.02.021.

[62] F. Carbone, M. Attoui, A. Gomez, Challenges of measuring nascent soot in flames as evidenced by high-resolution differential mobility analysis, Aerosol Sci. Technol. 50 (2016) 740–757. https://doi.org/10.1080/02786826.2016.1179715.

[63] R.C. Millikan, Optical Properties of Soot, J. Opt. Soc. Am. 51 (1961) 698–699. https://doi.org/10.1364/JOSA.51.000698.

[64] J. Simonsson, N.-E. Olofsson, S. Török, P.-E. Bengtsson, H. Bladh, Wavelength dependence of extinction in sooting flat premixed flames in the visible and near-infrared regimes, Appl. Phys. B. 119 (2015) 657–667. https://doi.org/10.1007/s00340-015-6079-z.

[65] M. Frenklach, J. Warnatz, Detailed Modeling of PAH Profiles in a Sooting Low-Pressure Acetylene Flame, Combust. Sci. Technol. 51 (1987) 265–283. https://doi.org/10.1080/00102208708960325.

[66] C. Saggese, A. V. Singh, X. Xue, C. Chu, M.R. Kholghy, T. Zhang, J. Camacho, J. Giaccai, J.H. Miller, M.J. Thomson, C.-J. Sung, H. Wang, The distillation curve and sooting propensity of a typical jet fuel, Fuel. 235 (2019) 350–362. https://doi.org/10.1016/j.fuel.2018.07.099.

[67] C. Saggese, A. Cuoci, A. Frassoldati, S. Ferrario, J. Camacho, H. Wang, T. Faravelli, Probe effects in soot sampling from a burner-stabilized stagnation flame, Combust. Flame. 167 (2016). https://doi.org/10.1016/j.combustflame.2016.02.013.

[68] C. Saggese, S. Ferrario, J. Camacho, A. Cuoci, A. Frassoldati, E. Ranzi, H. Wang, T. Faravelli, Kinetic modeling of particle size distribution of soot in a premixed burner-stabilized stagnation ethylene flame, Combust. Flame. 162 (2015). https://doi.org/10.1016/j.combustflame.2015.06.002.

[69] C. Liu, J. Camacho, H. Wang, Phase Equilibrium of TiO2 Nanocrystals in Flame-Assisted Chemical Vapor Deposition, ChemPhysChem. 19 (2018) 180–186. https://doi.org/10.1002/cphc.201700962.

[70] K.V. Puduppakkam, J. Camacho, A.U. Modak, H. Wang, C.V. Naik, E. Meeks, A soot chemistry model that captures fuel effects, in: Proc. ASME Turbo Expo, 2014. https://doi.org/10.1115/GT2014-27123.

[71] E.K.Y. Yapp, D. Chen, J. Akroyd, S. Mosbach, M. Kraft, J. Camacho, H. Wang, Numerical simulation and parametric sensitivity study of particle size distributions in a burner-stabilised stagnation flame, Combust. Flame. 162 (2015) 2569–2581. https://doi.org/10.1016/j.combustflame.2015.03.006.

[72] A.D. Abid, J. Camacho, D. a. Sheen, H. Wang, Evolution of Soot Particle Size Distribution Function in Burner-Stabilized Stagnation *n* -Dodecane−Oxygen−Argon Flames, Energy & Fuels. 23 (2009) 4286–4294. https://doi.org/10.1021/ef900324e.

[73] H. Lin, C. Gu, J. Camacho, B. Lin, C. Shao, R. Li, H. Gu, B. Guan, H. Wang, Z. Huang, Mobility size distributions of soot in premixed propene flames, Combust. Flame. 172 (2016). https://doi.org/10.1016/j.combustflame.2016.07.002.

[74] J. Camacho, S. Lieb, H. Wang, Evolution of size distribution of nascent soot in n- and i-butanol flames, Proc. Combust. Inst. 34 (2013) 1853–1860.

[75] P. Lespade, R. Al-Jishi, M.S. Dresselhaus, Model for Raman scattering from incompletely graphitized carbons, Carbon N. Y. 20 (1982) 427–431. https://doi.org/https://doi.org/10.1016/0008-6223(82)90043-4.

[76] M.A. Pimenta, G. Dresselhaus, M.S. Dresselhaus, L.G. Cancado, A. Jorio, R. Saito, Studying disorder in graphite-based systems by Raman spectroscopy, Phys. Chem. Chem. Phys. 9 (2007) 1276–1290. https://doi.org/10.1039/B613962K.

[77] A.C. Ferrari, Raman spectroscopy of graphene and graphite: Disorder, electron–phonon coupling, doping and nonadiabatic effects, Solid State Commun. 143 (2007) 47–57. https://doi.org/https://doi.org/10.1016/j.ssc.2007.03.052.

[78] M.S. Dresselhaus, G. Dresselhaus, Intercalation compounds of graphite, Adv. Phys. 30 (1981) 139–326. https://doi.org/10.1080/00018738100101367.

[79] F.. Tuinstra, J.L.. Koenig, Raman Spectrum of Graphite, J. Chem. Phys. 53 (1970) 1126–1130. https://doi.org/10.1063/1.1674108.

[80] A.C. Ferrari, J. Robertson, Resonant Raman spectroscopy of disordered, amorphous, and diamondlike carbon, Phys. Rev. B. 64 (2001) 75414. https://doi.org/10.1103/PhysRevB.64.075414.

[81] L.G. Cançado, K. Takai, T. Enoki, M. Endo, Y.A. Kim, H. Mizusaki, A. Jorio, L.N. Coelho, R. Magalhães-Paniago, M.A.

Pimenta, General equation for the determination of the crystallite size La of nanographite by Raman spectroscopy, Appl. Phys. Lett. 88 (2006) 163106. https://doi.org/10.1063/1.2196057.

[82] M.M. Lucchese, F. Stavale, E.H.M. Ferreira, C. Vilani, M.V.O. Moutinho, R.B. Capaz, C.A. Achete, A. Jorio, Quantifying ion-induced defects and Raman relaxation length in graphene, Carbon N. Y. 48 (2010) 1592–1597. https://doi.org/https://doi.org/10.1016/j.carbon.2009.12.057.

[83] E.H. Martins Ferreira, M.V.O. Moutinho, F. Stavale, M.M. Lucchese, R.B. Capaz, C.A. Achete, A. Jorio, Evolution of the Raman spectra from single-, few-, and many-layer graphene with increasing disorder, Phys. Rev. B. 82 (2010) 125429. https://doi.org/10.1103/PhysRevB.82.125429.

[84] L.G. Cançado, A. Jorio, E.H.M. Ferreira, F. Stavale, C.A. Achete, R.B. Capaz, M.V.O. Moutinho, A. Lombardo, T.S. Kulmala, A.C. Ferrari, Quantifying Defects in Graphene via Raman Spectroscopy at Different Excitation Energies, Nano Lett. 11 (2011) 3190–3196. https://doi.org/10.1021/nl201432g.

[85] H. Marsh, A tribute to Philip L. Walker, Carbon N. Y. 29 (1991) 703–704. https://doi.org/https://doi.org/10.1016/0008-6223(91)90004-3.

[86] I.C. Lewis, Chemistry of carbonization, Carbon N. Y. 20 (1982) 519–529. https://doi.org/http://dx.doi.org/10.1016/0008-6223(82)90089-6.

[87] R.A. Dobbins, G.J. Govatzidakis, W. Lu, A.F. Schwartzman, R.A. Fletcher, Carbonization Rate of Soot Precursor Particles, Combust. Sci. Technol. 121 (1996) 103–121. https://doi.org/10.1080/00102209608935589.

[88] E.F. Antunes, A.O. Lobo, E.J. Corat, V.J. Trava-Airoldi, A.A. Martin, C. Veríssimo, Comparative study of first- and second-order Raman spectra of MWCNT at visible and infrared laser excitation, Carbon N. Y. 44 (2006) 2202–2211. https://doi.org/https://doi.org/10.1016/j.carbon.2006.03.003.

[89] P. Minutolo, M. Commodo, A. Santamaria, G. De Falco, A. D'Anna, Characterization of flame-generated 2-D carbon nano-disks, Carbon N. Y. 68 (2014) 138–148. https://doi.org/https://doi.org/10.1016/j.carbon.2013.10.073.